Check for updates

*Advanced Electronic Materials*

ADVANCED ELECTRONIC MATERIALS Open Access

www.advelectronicmat.de

RESEARCH ARTICLE OPEN ACCESS

# Reduced Variability in Threshold Switches Using Heterostructures of $SiO_x$ and Vertically Aligned $MoS_2$

Jimin Lee[1] | Rana Walied Ahmad[2] | Sofía Cruces[1] | Dennis Braun[1] | Lukas Völkel[1] | Ke Ran[3,4,5] | Joachim Mayer[4,5] | Stephan Menzel[2] | Alwin Daus[1,6] | Max C. Lemme[1,3]

[1]Chair of Electronic Devices, RWTH Aachen University, Aachen, Germany | [2]JARA-Fit and Peter Grünberg Institute (PGI-7), Forschungszentrum Jülich GmbH, Jülich, Germany | [3]Advanced Microelectronic Center Aachen, AMO GmbH, Aachen, Germany | [4]Central Facility for Electron Microscopy, RWTH Aachen University, Aachen, Germany | [5]Ernst Ruska Centre for Microscopy and Spectroscopy with Electrons, Forschungszentrum Jülich GmbH, Jülich, Germany | [6]Institute of Semiconductor Engineering, University of Stuttgart, Stuttgart, Germany

**Correspondence:** Max C. Lemme (max.lemme@eld.rwth-aachen.de)

**Received:** 6 November 2025 | **Revised:** 31 January 2026 | **Accepted:** 3 March 2026

**Keywords:** conductive filaments | heterostructure | memristive devices | threshold switching | variability-aware simulations | vertically aligned molybdenum disulfide

## ABSTRACT

Two-dimensional (2D) materials and their heterostructures offer promising pathways for intercalated ion migration and regulated filament growth in resistive switching (RS) devices, enabled by their van der Waals (vdW) gaps. In vertically aligned 2D materials, this vdW gap-mediated ion transport holds great potential for high-density integration and reliable RS performance for memristor crossbar arrays. However, the fundamental switching mechanisms and their contributions to the RS remain inadequately understood. In this work, we investigate silver (Ag) filament-based threshold switching (TS) in heterostructures comprising vertically aligned 2D molybdenum disulfide ($VAMoS_2$) grown via sulfurization and silicon oxide ($SiO_x$). Compared to $SiO_x$-only devices, the $SiO_x/VAMoS_2$ devices exhibit TS with higher on-threshold and hold voltages, each approximately 0.4 V, faster switching times down to 356 ns under a 4 V pulse, and a lower cycle-to-cycle on-current variability of 3.0%. A physics-based, variability-aware model reveals that confined Ag ion migration within the vdW gaps in $VAMoS_2$ forms ultrathin seed filaments, which guide filament growth in the $SiO_x$ layer. These findings establish $SiO_x/VAMoS_2$ heterostructures as a promising concept for reliable TS in vertical device architectures for emerging memories and neuromorphic computing.

## 1 | Introduction

Two-dimensional (2D) materials have gained attention as resistive switching (RS) media for neuromorphic and in-memory computing applications [1–4]. Various 2D materials, including transition metal dichalcogenides (TMDs) [5–7], hexagonal boron nitride (h-BN) [8–10], 2D heterostructures [11–13], and oxide-2D heterostructures [14–17], have shown memristive RS characteristics. 2D materials can be stacked vertically with other materials without requiring lattice matching [18], which enables multifunctional 3D integration [19]. This capability opens opportunities for compact, high-performance memory and computing technologies based on 2D material memristive devices [6, 20].

Two-terminal memristive devices based on 2D materials, consisting of a metal-2D-metal configuration, are particularly attractive for energy-efficient technologies because of their small footprint, high integration density, and low switching energy [1, 5]. Recently, vertically aligned 2D materials have emerged as promising RS media for such vertical two-terminal devices [19, 21–25]. For example, vertically aligned h-BN grown by plasma-enhanced chemical vapor deposition has shown nonvolatile RS with a high

This is an open access article under the terms of the Creative Commons Attribution License, which permits use, distribution and reproduction in any medium, provided the original work is properly cited.

© 2026 The Author(s). *Advanced Electronic Materials* published by Wiley-VCH GmbH

device yield of ~90%, multistate conductance, and compatibility with complementary metal oxide semiconductor technology [19]. Vertically aligned 2D molybdenum disulfide ($VAMoS_2$) grown by chemical vapor deposition (CVD) has shown volatile RS with an on/off ratio of ~$10^6$, enabling artificial neuron emulation [23]. Nonvolatile RS has also been observed in $VAMoS_2$ on silicon (Si) with chromium (Cr)/gold (Au) electrodes, where switching is caused by hydroxyl ions originating from the catalytic splitting of adsorbed water molecules [21]. The heterostructures of $VAMoS_2$ and silicon oxide ($SiO_x$) have further demonstrated silver (Ag)-based filamentary threshold RS with endurance exceeding $10^4$ cycles [26]. These findings highlight the potential of vertically aligned 2D materials for use in memristive devices; however, their switching mechanisms or their roles in the RS behavior of heterostructures remain insufficiently understood, e.g., on the influence of the vertical alignment of 2D materials or their presence in heterostructures on key performance parameters such as the switching speed, variability, and reliability.

Memristive devices change their electrical resistance in response to an applied voltage [27]. One of the predominant RS mechanisms is electrochemical-metallization (ECM) [28, 29], where metallic filaments form and dissolve within the switching medium due to the migration of active metal ions such as Ag, copper (Cu), or nickel (Ni) [11, 30–32]. The formation and dissolution of conductive filaments (CFs) are inherently stochastic, controlled by the electric field, the switching medium, and the electrode interface, all of which influence filament stability and morphology [9, 11, 33]. Thick and bulky CFs typically result in nonvolatile RS, whereas thin and fragile CFs rupture spontaneously after bias removal, leading to volatile RS, also known as threshold switching (TS), observed in diffusive memristors [28, 33, 34]. In 2D materials, ECM-based RS is driven by ion migration along intrinsic structural features such as van der Waals (vdW) gaps, grain boundaries, and defects [22, 35–41]. Since 2D materials play a crucial role in determining the switching dynamics, material selection and device configuration must be considered when optimizing the device performance.

In this work, we compare Ag filament-based TS in vertical memristive devices consisting of $SiO_x$ with and without $VAMoS_2$ layers. We elucidate the influence of the $VAMoS_2$ layers on the TS behavior, with a particular focus on the switching dynamics based on filament formation, by combining experimental data with a physics-based JART ECM simulation model [42–44]. The presence of the $VAMoS_2$ layer regulates Ag ion migration through its vdW gaps, leading to confined filament formation with faster switching speeds and slightly higher average switching voltages with significantly lower cycle-to-cycle variability compared to devices based on $SiO_x$ alone.

## 2 | Results and Discussion

### 2.1 | Device Fabrication and Structure

Our devices consist of a vertical stack with an active Ag top electrode (TE) and an inert Au bottom electrode (BE). The switching medium is either a $SiO_x/VAMoS_2$ heterostructure or a $SiO_x$ layer ($SiO_x$-only), as shown in Figure 1a,b. These configurations allow us to investigate the influence of the $VAMoS_2$ layer on the RS behavior during CF formation.

Device fabrication began with the patterning of Au BEs on a Si substrate covered with a 300 nm thick thermal $SiO_2$ film using photolithography, e-beam evaporation, and lift-off. For heterostructure devices, a 6 nm molybdenum (Mo) film was then sputtered and patterned on the predefined Au BEs. The $VAMoS_2$ layer was synthesized by sulfurizing the Mo film in a sulfur atmosphere at 800°C [26, 45]. During this process, an amorphous $SiO_x$ layer formed on the $VAMoS_2$ surface by diffusion of Si and O from the substrate [26, 46, 47]. For $SiO_x$-only devices, a comparable $SiO_x$ layer was formed on the Au BEs without a Mo film but otherwise under identical fabrication conditions. Finally, the Ag TE, capped with an Au layer, was patterned via photolithography, e-beam evaporation, and lift-off. Detailed descriptions of the device fabrication and material growth processes are provided in Section 4.1 of the Methods section.

Cross-sectional transmission electron microscopy (TEM) confirmed the device stacks (see Figure S1). Energy-dispersive X-ray spectroscopy (EDXS) elemental mapping verified the presence of Si, O, Mo, and S in the heterostructure between the Ag TE and the Au BE (Figure 1c) and comparable Si and O signals in the $SiO_x$-only device (Figure 1d). High-resolution TEM (HRTEM) imaging revealed the vertical alignment of the $MoS_2$ layers in the $SiO_x/VAMoS_2$ device (Figure 1e). Raman spectroscopy confirmed the crystalline 2H-phase of $MoS_2$, with characteristic peaks at 382 $cm^{-1}$ and 407 $cm^{-1}$, corresponding to the $E^1_{2g}$ and $A_{1g}$ modes, respectively (Figure 1f) [48]. The $E^1_{2g}/A_{1g}$ peak intensity ratio of ~0.4 further supported the vertical orientation of $MoS_2$ [49].

### 2.2 | Direct-Current (dc) Characterization

Direct-current (dc) current–voltage ($I$–$V$) measurements were performed on $SiO_x/VAMoS_2$ and $SiO_x$-only devices by applying a bias voltage to the Ag TE while grounding the BE. A current compliance ($I_{cc}$) of 1 μA was set for the measurements. Both devices exhibited reproducible TS over 128 consecutive cycles without requiring an initial electroforming step (Figure 2a,b). The $SiO_x/VAMoS_2$ device showed gradual current transitions, whereas the $SiO_x$-only device showed abrupt transitions. During the forward sweep, both devices switched from the initial high-resistance state (HRS) to the low-resistance state (LRS) at the on-threshold voltage ($V_{t,on}$). In the reverse sweep, the devices remained in the LRS until the voltage dropped below the hold voltage ($V_{hold}$), after which they returned to the HRS. The off-threshold voltage ($V_{t,off}$) was defined as the voltage at which the current returned to the initial HRS current level, using a fixed 100 pA criterion.

We extracted the switching voltage parameters ($V_{t,on}$, $V_{hold}$, and $V_{t,off}$) from 128 consecutive switching cycles of the $SiO_x/VAMoS_2$ and $SiO_x$-only devices. The distributions of the parameters are shown as histograms and cycle-dependent plots in Figures S2 and S3. Compared with the $SiO_x$-only devices, the $SiO_x/VAMoS_2$ devices showed smaller fluctuations in all three voltage parameters. For example, the $V_{t,on}$ values of the $SiO_x/VAMoS_2$ device ranged from 0.3 to 0.5 V, whereas those of the $SiO_x$-only device



2199160x, 0, Downloaded from https://advanced.onlinelibrary.wiley.com/doi/10.1002/aelm.202500800 by Universitatsbibliothek RWTH Aachen University, Wiley Online Library on [24/03/2026]. See the Terms and Conditions (https://onlinelibrary.wiley.com/terms-and-conditions) on Wiley Online Library for rules of use; OA articles are governed by the applicable Creative Commons License

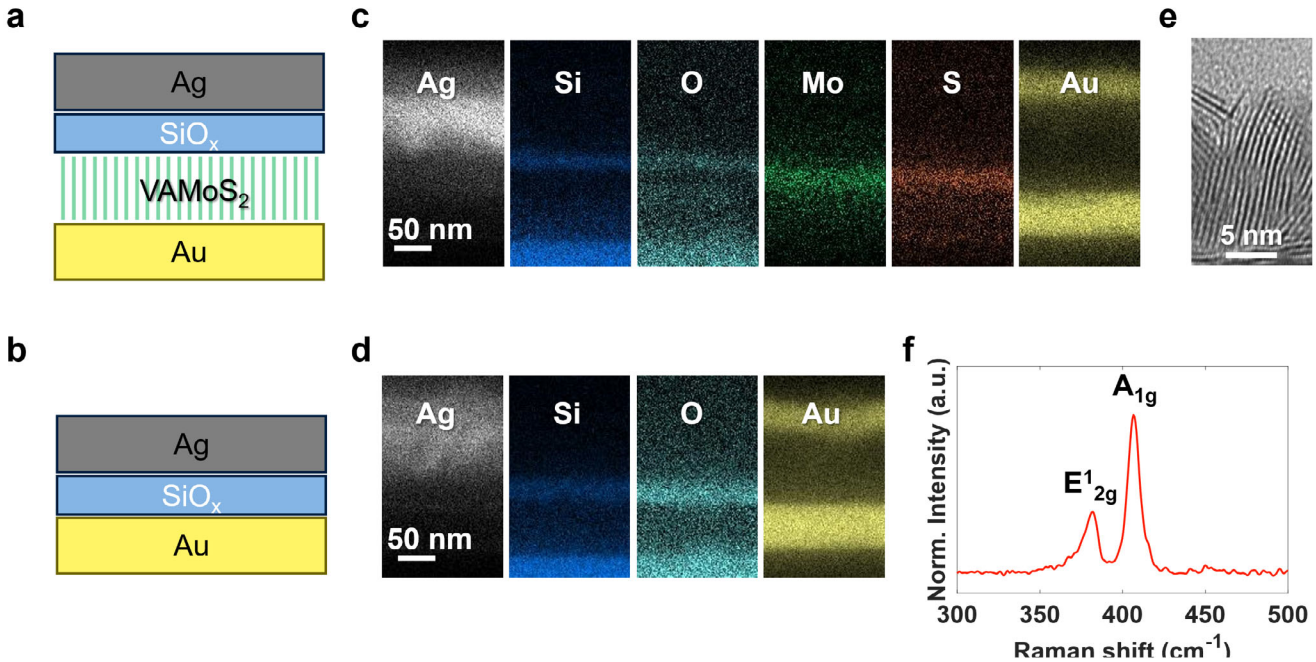


**FIGURE 1** | Device Structures and Materials Characterization. Schematic cross-sections of the switching layers of (a) a $SiO_x/VAMoS_2$ and (b) a $SiO_x$-only device between the top (Ag) and bottom (Au) electrodes. EDXS elemental mapping confirming the presence of (c) Ag, Si, O, Mo, S, and Au in the $SiO_x/VAMoS_2$ device and (d) Ag, Si, O, and Au in the $SiO_x$-only device. (e) HRTEM cross-section revealing the vertically layered structure of $MoS_2$. (f) Raman spectrum of an as-grown $MoS_2$ film on an Au surface verifying the crystalline 2H-phase of $MoS_2$ with its characteristic $E^1_{2g}$ (382 $cm^{-1}$) and $A_{1g}$ (407 $cm^{-1}$) modes.

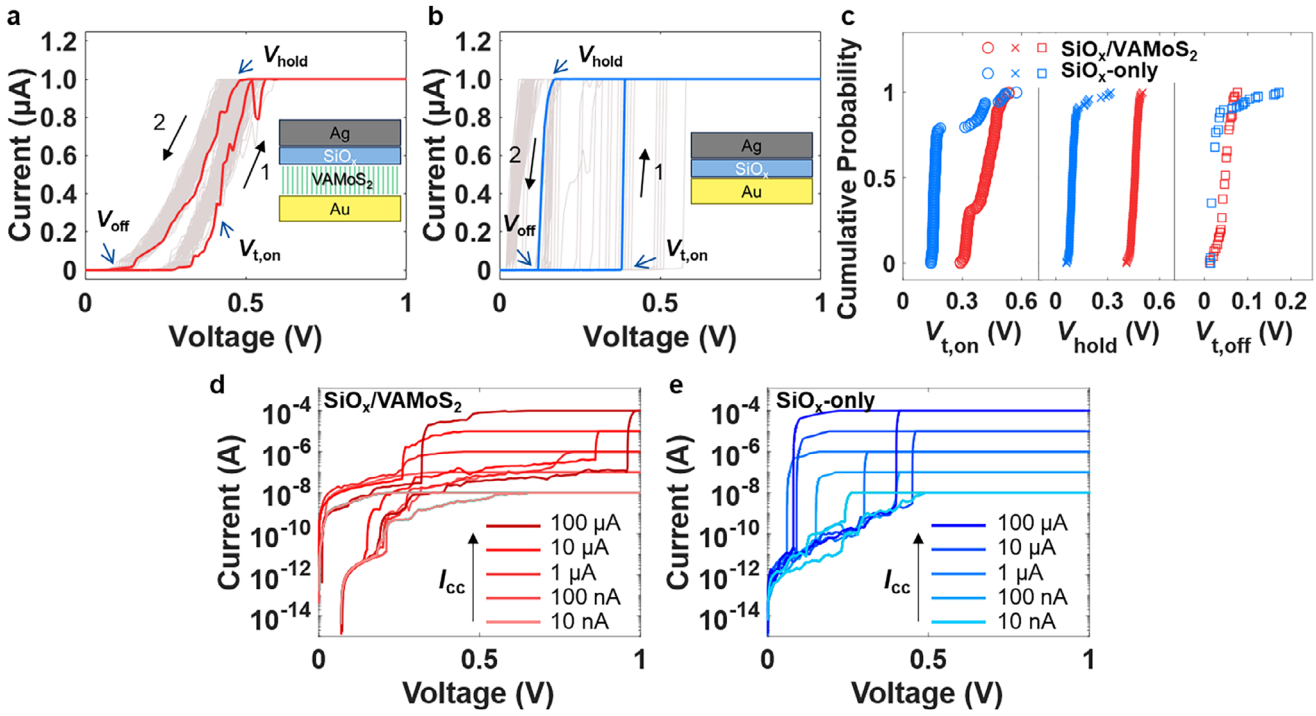


**FIGURE 2** | Threshold Switching Characteristics of $SiO_x/VAMoS_2$ and $SiO_x$-only Devices. (a) 128 consecutive dc *I–V* sweeps for the $SiO_x/VAMoS_2$ device at $I_{cc} = 1$ μA, showing a gradual current transition. The first sweep is marked in red. Inset: schematic cross-section of the $SiO_x/VAMoS_2$ device. (b) 128 consecutive *I–V* sweeps for the $SiO_x$-only device, showing abrupt transitions. The first sweep is marked in blue. Inset: schematic cross-section of the $SiO_x$-only device. Characteristic voltages are indicated on the curves in (a) and (b). (c) Cumulative distribution functions of $V_{t,on}$, $V_{hold}$, and $V_{t,off}$ extracted from the data displayed in (a) and (b). Five subsequent *I–V* sweeps under different $I_{cc}$ values (10 nA to 100 μA) showing the TS in (d) the $SiO_x/VAMoS_2$ device and (e) the $SiO_x$-only device.



2199160x, 0, Downloaded from https://advanced.onlinelibrary.wiley.com/doi/10.1002/aelm.202500800 by Universitatsbibliothek RWTH Aachen University, Wiley Online Library on [24/03/2026]. See the Terms and Conditions (https://onlinelibrary.wiley.com/terms-and-conditions) on Wiley Online Library for rules of use; OA articles are governed by the applicable Creative Commons License

varied widely between 0.1 and 0.6 V. The normalized cumulative distribution functions (CDFs) of $V_{t,on}$, $V_{hold}$, and $V_{t,off}$ over 128 cycles show that the presence of the $VAMoS_2$ layer increases the average switching voltage while reducing the cycle-to-cycle variability (Figure 2c). A certain degree of variability remaining in the $SiO_x/VAMoS_2$ devices may be attributed to the microstructure of $VAMoS_2$. Structural features such as orientation variations, defects, and grain boundaries may act as localized diffusion pathways, contributing to the stochastic behavior of filament formation and rupture. The vertically aligned vdW gaps in the $VAMoS_2$ layers provide predefined ion migration pathways, which may promote confined and reproducible formation and rupture of the CFs [22, 39, 40, 50]. The average $V_{hold}$ also increased from $0.1 \pm 0.04$ V in $SiO_x$-only to $0.4 \pm 0.02$ V in the $SiO_x/VAMoS_2$ heterostructure, indicating easier rupture of the CFs in the heterostructure, which is potentially due to a structurally weak point at the $SiO_x/VAMoS_2$ interface. The devices returned to their initial HRS at $V_{t,off}$ of $\sim 0.05 \pm 0.01$ V for the heterostructure devices and $\sim 0.03 \pm 0.03$ V for the $SiO_x$-only devices.

Figure 2d,e shows the TS in both device types for different $I_{cc}$ values, i.e., over four orders of magnitude from 10 nA to 100 μA. The $SiO_x/VAMoS_2$ device exhibited stepwise switching, with an initial abrupt current increase followed by a gradual rise (Figure 2d), whereas the $SiO_x$-only device showed sharp and abrupt transitions once $V_{t,on}$ was reached (Figure 2e). While the origin of the stepwise switching in the $SiO_x/VAMoS_2$ device remains to be fully elucidated, several factors may contribute to this phenomenon, including multi-seed Ag nucleation forming parallel conductive segments, interfacial redox reactions leading to incremental filament growth, partial filament bridging or rupture within vdW gaps, filament branching induced by structural inhomogeneities. Similar mechanisms have been reported in ECM-based memristive devices [40, 51–54]. Despite the need for further investigation, the device exhibits high on-state current and reproducible TS behavior, suggesting its potential for selector applications [55, 56] and neuromorphic computing, particularly for implementing artificial neurons [23].

## 2.3 | Pulsed Voltage Characterization

Pulsed voltage measurements were conducted to explore the transient switching dynamics. The time-dependent current response was recorded under voltage pulses of varying amplitudes ($V_{pulse}$). As shown in Figure 3a, the switching time ($t_{on}$) corresponds to the time required for the current to reach 90% of the on-current ($I_{on}$) [26, 41]. For each measurement, a voltage pulse was applied to switch the device from the HRS to the LRS within $t_{on}$, after which the device spontaneously returned to the HRS. The HRS level was quantified as the off-current ($I_{off}$) by using a subsequent read pulse of 0.3 V ($V_{read}$) with a duration of 3 μs. The on- and off-switching characteristics are described in detail in the literature [26, 41]. Figure 3a shows a representative transient response of the $SiO_x/VAMoS_2$ device to a 4 V pulse with a duration of 2 μs. The inset presents the corresponding applied voltage pulse waveform. Varying the pulse duration between 1 and 3 μs had no influence on the switching dynamics (Figure S4).

We plotted the $I_{on}$ and $I_{off}$ values from 30 consecutive cycles of a $V_{pulse}$ of 4 V for 2 μs for a $SiO_x/VAMoS_2$ and a $SiO_x$-only device (Figure 3b,c). The heterostructure device had significantly lower variations in $I_{on}$ (3.0%) compared to the $SiO_x$-only device (46.5%). The $t_{on}$ values were fitted with Gaussian distributions with mean values (μ) and standard deviations (σ) of 620 and 160 ns for the $SiO_x/VAMoS_2$ and 940 and 450 ns for the $SiO_x$-only device (Figure 3d). The broader $t_{on}$ distribution of the $SiO_x$-only devices reflects higher variability. Given that the switching dynamics can be modulated by the voltage amplitude [11, 29, 33] and that $t_{on}$ is a critical parameter in memristive device operation [57, 58], we investigated the dependence of $t_{on}$ on $V_{pulse}$ by applying 30 consecutive pulses. Compared with the $SiO_x$-only device, the $SiO_x/VAMoS_2$ device demonstrated relatively faster $t_{on}$ values with reduced variations across amplitudes of 4, 4.5, and 5 V (Figure S5). Next, we plotted the on-state resistance ($R_{on}$) as a function of $V_{pulse}$ for both device types (Figure 3e). Compared with the $SiO_x$-only devices, the $SiO_x/VAMoS_2$ devices exhibited lower average $R_{on}$ values with reduced cycle-to-cycle variability. These results suggest that the vertically aligned vdW gaps in the $VAMoS_2$ confine ion migration [21, 22, 39, 40], leading to controlled filament growth and rupture, faster switching speeds, and reduced variability. Furthermore, the $R_{on}$ values decreased with increasing amplitude of $V_{pulse}$ for both devices, which is consistent with stronger Ag ion drift, enhanced CF formation, and increased current flow at higher pulse amplitudes [59]. In Section 2.4, we further discuss the switching variability and filament formation mechanisms by correlating the experimentally observed data with the physics-based JART ECM simulation model [42–44] and by comparing devices with and without the $VAMoS_2$ layer.

## 2.4 | Conductive Filament Formation and Variability Modeling

Figure 4a shows schematic cross-sections of our proposed CF formation process in $SiO_x/VAMoS_2$ and $SiO_x$-only devices in the LRS. In both devices, applying a positive bias to the Ag TE induces oxidation of Ag, generating Ag ions that migrate toward the Au BE. Upon reaching the BE, the Ag ions are reduced and form a metallic nucleation seed at the interface between the switching medium and the BE [43, 60]. The seed initiates the growth of the CFs upward from the BE toward the TE, switching the device from the HRS to the LRS [43]. In the $SiO_x/VAMoS_2$ devices, the vdW gaps in the $VAMoS_2$ layers function as ion-conducting channels that confine Ag ion migration [22, 39, 40], leading to the nucleation of ultrathin seed filaments at the BE and their subsequent extension along the vdW gaps. The $VAMoS_2$ layer thus directs and restricts filament growth. At the $SiO_x/VAMoS_2$ interface, the pre-confined seed filaments provide favorable points that promote extension into the overlying $SiO_x$ layer, where the seed filaments can drive the development of thicker filaments in the $SiO_x$ layer. In contrast, the $SiO_x$-only devices lack such guided pathways, which leads to randomly initiated thin filaments that form directly from the Au BE. Notably, in both device types, the CFs remain sufficiently thin to rupture spontaneously, enabling TS.

Figure 4b,c shows the transient current responses of a $SiO_x/VAMoS_2$ and a $SiO_x$-only device, respectively, under a $V_{pulse} = 4$ V for a duration of 2 μs, which was repeated for 30 cycles. These experimental data confirm faster and more consistent switching in the $SiO_x/VAMoS_2$ heterostructure



2199160x, 0, Downloaded from https://advanced.onlinelibrary.wiley.com/doi/10.1002/aelm.202500800 by Universitatsbibliothek RWTH Aachen University, Wiley Online Library on [24/03/2026]. See the Terms and Conditions (https://onlinelibrary.wiley.com/terms-and-conditions) on Wiley Online Library for rules of use; OA articles are governed by the applicable Creative Commons License

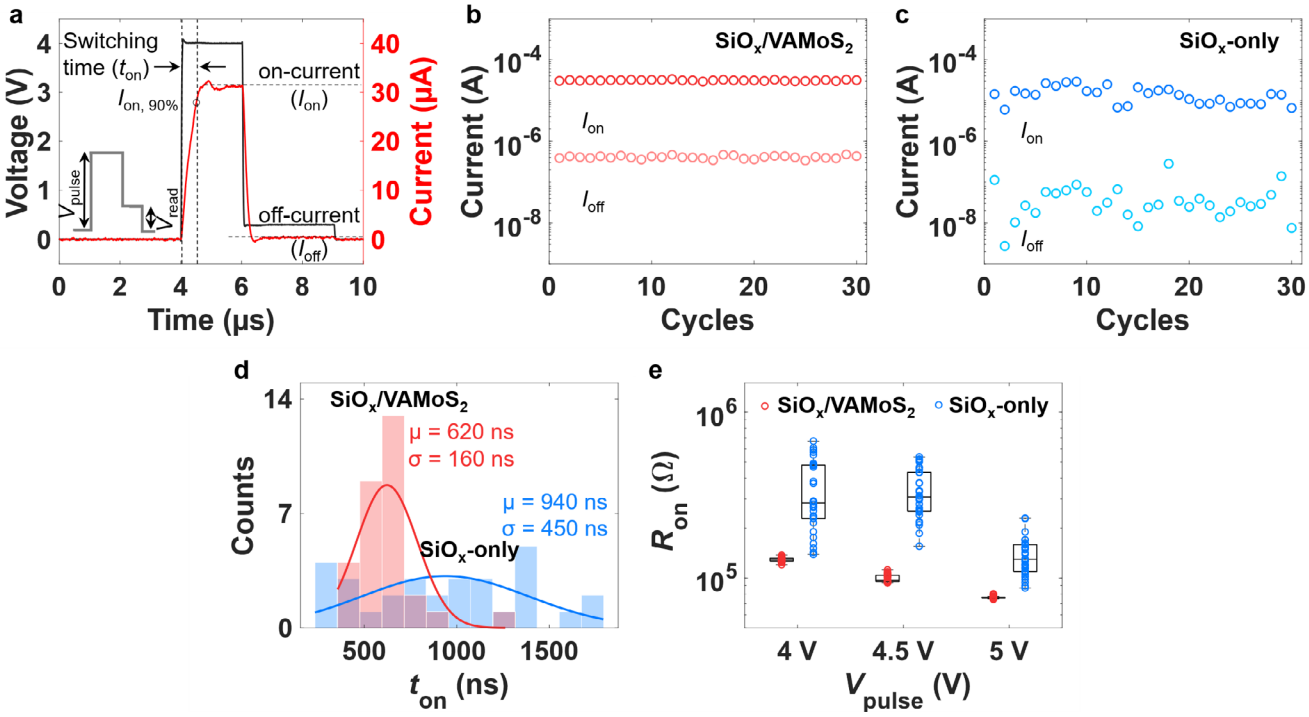


**FIGURE 3** | Switching dynamics of $SiO_x/VAMoS_2$ and $SiO_x$-only devices. (a) Representative transient response of a $SiO_x/VAMoS_2$ device under a voltage pulse of 4 V/2 μs, followed by a read pulse of 0.3 V/3 μs. The inset shows the applied waveform. On-current ($I_{on}$) and off-current ($I_{off}$) values extracted over 30 consecutive switching cycles for (b) a $SiO_x/VAMoS_2$ and (c) a $SiO_x$-only device. (d) Cycle-to-cycle variability of the switching time ($t_{on}$) over 30 pulses at 4 V, showing faster average and more reproducible switching in the $SiO_x/VAMoS_2$ device ($\mu = 620$ ns, $\sigma = 160$ ns) than in the $SiO_x$-only device ($\mu = 940$ ns, $\sigma = 450$ ns). (e) On-state resistance ($R_{on}$) as a function of pulse amplitude, with lower average values and reduced variability in the $SiO_x/VAMoS_2$ device than in the $SiO_x$-only device.

than in the $SiO_x$-only device. A physics-based, variability-aware ECM model [43] reproduced the experimental data for the $SiO_x/VAMoS_2$ and $SiO_x$-only devices via a cycle-to-cycle variability fit, as shown in Figure 4d,e. Details of the model are provided in Section 4.4 of the Methods section, and the fitting parameters are summarized in Table S1 in Supplementary Section S6. The model achieved good agreement with the experimental data, successfully capturing the faster $t_{on}$ and narrower $t_{on}$ distributions observed in the $SiO_x/VAMoS_2$ devices.

The simulations suggest that the variability originates from the filament radius ($r_{fil}$) and the stochastic distance ($x$) between the filament tip and the TE. In heterostructure devices, the interlayer gap of the $VAMoS_2$ layers forms ultrathin filaments, estimated to be only 1–2 vdW gaps wide. The gap spacing of ~6.5 Å [22, 61] exceeds the Ag atomic diameter of 3.44 Å [62], which allows confined ion migration. The filament in $VAMoS_2$ is restricted and mainly experiences vertical growth along a vdW gap [22, 39]. Hence, it is assumed that the filament does not substantially grow in the horizontal direction within $VAMoS_2$ after nucleation. Thus, the diameter of the ultrathin filament within $VAMoS_2$ is as small as the diameter of the nucleus at the $VAMoS_2$/Au interface. These ultrathin filaments in $VAMoS_2$ ($r_{fil(1,VAMoS2)}$) subsequently extend into the $SiO_x$ layer, where they seed the growth of thicker filaments in the $SiO_x$ layer ($r_{fil(1,SiOx)} > r_{fil(1,VAMoS2)}$). In the $SiO_x$-only devices, filaments nucleate randomly at the Au/$SiO_x$ interface with radii larger than those in the $VAMoS_2$ region but smaller than those in the $SiO_x$ region of the heterostructure devices ($r_{fil(1,SiOx)} > r_{fil(2,SiOx)} > r_{fil(1,VAMoS2)}$, see Figure 4a). In the $SiO_x$-only devices, the subsequent filament diameter in $SiO_x$ is not coupled to the nucleus diameter at the Au/$SiO_x$ interface and grows with larger diameters.

Thus, the pre-confined seeds at the $SiO_x/VAMoS_2$ interface play a critical role in initiating thicker and more reproducible filament growth in the $SiO_x$ layers of the heterostructures. The cycle-to-cycle variability model further showed that the filament radius is closely linked to the stochastic parameter $\delta$, describing the stochastic change in the distance $x$ between the filament tip and TE. A larger filament corresponds to smaller variability and to a smaller $\delta$ because the addition or removal of single atoms does not strongly affect the filament geometry and the current through it. Conversely, a narrow filament displays higher variability and a larger $\delta$, as single-atom changes significantly alter the filament geometry and the electronic current, according to the exponential relation of $x$ in the electronic tunneling current. Owing to stochasticity, discrete current jumps occur as a few atoms are added or removed from the filament tip at random intervals, modifying the minimum distance between the filament tip and TE and the current response.

We attribute the improved TS performance to the $VAMoS_2$ layer directing thin CF growth and providing a structurally weak point at the $SiO_x/VAMoS_2$ interface, where it easily breaks. Our results align with previous findings where restricting Ag ion transport through atomic defects in graphene reduced the number of ions entering the switching medium [11].



2199160x, 0, Downloaded from https://advanced.onlinelibrary.wiley.com/doi/10.1002/aelm.202500800 by Universitatsbibliothek RWTH Aachen University, Wiley Online Library on [24/03/2026]. See the Terms and Conditions (https://onlinelibrary.wiley.com/terms-and-conditions) on Wiley Online Library for rules of use; OA articles are governed by the applicable Creative Commons License

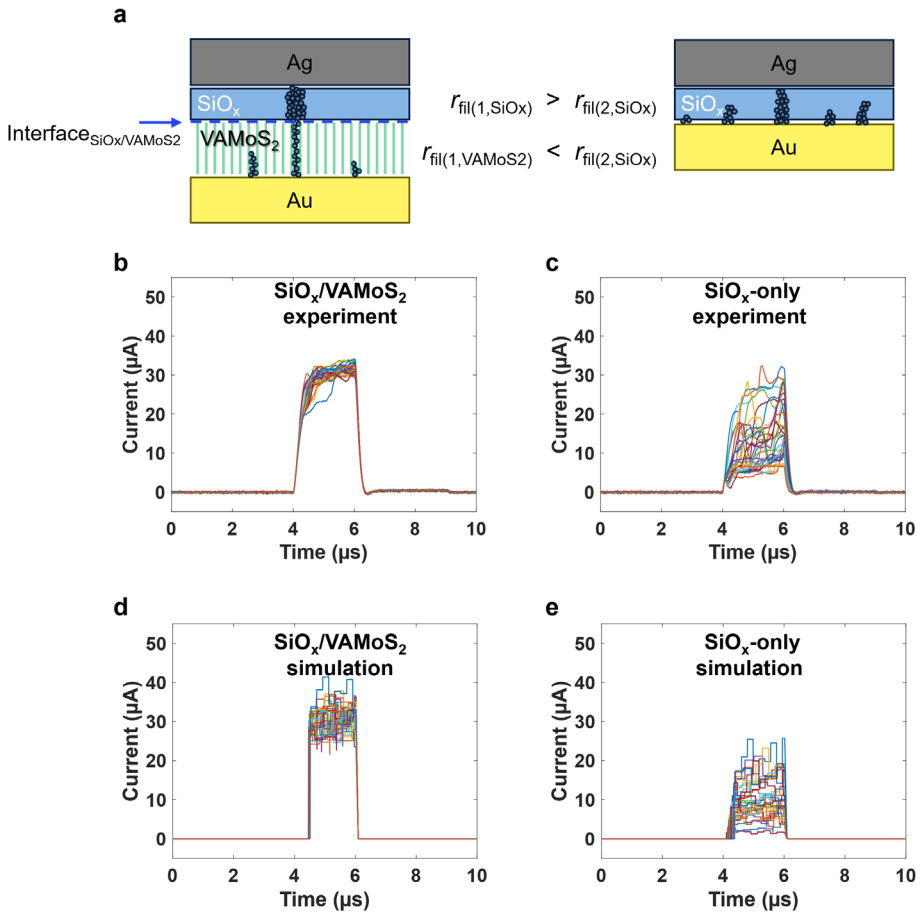


**FIGURE 4** | Filament Formation and Variability Modeling in $SiO_x/VAMoS_2$ and $SiO_x$-only Devices. (a) Schematic of conductive filament (CF) growth in the LRS: in $SiO_x/VAMoS_2$, vdW gaps guide ultrathin Ag seed CFs at the BE that extend into the $SiO_x$ layer, whereas in the $SiO_x$-only device, CFs nucleate randomly at the BE. Transient current responses under repeated 4 V/2 μs pulses over 30 cycles, showing faster and more consistent switching in (b) a $SiO_x/VAMoS_2$ device than in (c) a $SiO_x$-only device. Cycle-to-cycle variability fitting via the JART ECM model [42–44], reproducing the experimental data for (d) the $SiO_x/VAMoS_2$ and (e) the $SiO_x$-only devices.

## 3 | Conclusion

We compared Ag filament-based TS in vertical, two-terminal devices comprising $SiO_x/VAMoS_2$ and $SiO_x$ as switching layers. Compared with the $SiO_x$-only devices, the $SiO_x/VAMoS_2$ devices showed enhanced switching characteristics, including faster switching times, higher $V_{hold}$ with significantly reduced variability, and more stable and repeatable transient current responses. Our study suggests that these improvements originate from the vdW gaps in the $VAMoS_2$ layers, which guide and confine Ag ion migration. This confinement enables the formation of ultrathin seed filaments that extend into the overlying $SiO_x$, where they initiate stable conductive pathways. The combination of electrical and analytical experiments with physics-based ECM simulations confirms that the filament morphology determines the switching dynamics and variability. In particular, the pre-confined seed filaments at the $SiO_x/VAMoS_2$ interface establish a well-controlled environment for filament growth, leading to more reliable TS behavior. These findings show that vertically aligned 2D materials offer an effective strategy for engineering CF formation in memristive devices and suggest their strong potential in emerging memory and neuromorphic computing applications.

## 4 | Methods

### 4.1 | Device Fabrication and Material Growth

Devices with lateral dimensions of 4 μm x 4 μm were fabricated on Si chips (2 cm x 2 cm) covered with 300 nm thermal $SiO_2$. The bottom electrodes (BEs) were patterned via a double resist stack (LOR 3A/AZ5214E from MicroChemicals GmbH/Merck Performance Materials GmbH) and optical contact lithography with an EVG 420 mask aligner. A 5 nm Ti adhesion layer and a 50 nm Au layer were deposited via electron-beam evaporation in a Pfeiffer tool and lifted off in dimethyl sulfoxide (DMSO) heated to 80°C. The Mo films were patterned via the same double resist stack and lithography process. A 6 nm Mo layer was deposited via dc sputtering with the CREAVAC tool (CREAMET S2) and lifted off in DMSO. For $SiO_x$-only devices, Au BEs without Mo patterns were retained on the same chip. $SiO_x/VAMoS_2$ and $SiO_x$ stacks were synthesized on Mo/Au BEs and Au BEs, respectively, by sulfurization in a CVD tube furnace (RS 80/300, Nabertherm GmbH). $VAMoS_2$ layers were formed by thermally assisted conversion of Mo in a sulfur atmosphere at 800°C for 30 min with an Ar carrier gas (20 sccm) at a pressure of 9.6 $\times 10^{-2}$ mbar [26]. Sulfur diffusion converted the Mo film into



2199160x, 0, Downloaded from https://advanced.onlinelibrary.wiley.com/doi/10.1002/aelm.202500800 by Universitatsbibliothek RWTH Aachen University, Wiley Online Library on [24/03/2026]. See the Terms and Conditions (https://onlinelibrary.wiley.com/terms-and-conditions) on Wiley Online Library for rules of use; OA articles are governed by the applicable Creative Commons License

~20 nm thick $VAMoS_2$ layers, while ~10 nm of amorphous $SiO_x$ simultaneously formed on top of the $VAMoS_2$/Au BE stacks in the $SiO_x$/$VAMoS_2$ devices and directly on the Au BEs in the $SiO_x$-only devices. Finally, the top electrodes (TEs) were defined via the same lithography process as the BE. A 30 nm Ag layer capped with a 30 nm Au layer was deposited via electron-beam evaporation, followed by lift-off.

### 4.2 | Material Characterization

Transmission electron microscopy (TEM) analysis was carried out to investigate the cross-sectional device structure, the orientation of the $MoS_2$ layers, and the chemical composition. TEM lamellae were prepared via a focused ion beam (FIB) in an FEI Strata400 system. TEM imaging and energy-dispersive X-ray spectroscopy (EDXS) were conducted with a JEOL JEM F200 instrument operated at 200 kV. Raman measurements were conducted via a WITec alpha 300R Raman system with a 532 nm excitation laser operating at 1 mW power and an 1800 g/mm grating.

### 4.3 | Electrical Characterization

Electrical measurements were conducted under ambient conditions at room temperature using a Lakeshore probe station connected to a semiconductor parameter analyzer (Keithley 4200S-SCS, Tektronix) equipped with two source measure unit (SMU) cards (Keithley 4200-SMU) and preamplifiers (Keithley 4200-PA). A voltage bias was applied to the Ag TE, and the Au BE was grounded. The applied voltage was monitored from the Ag TE, and the output current was recorded from the Au BE. For dc voltage sweeps, the voltage was applied from 0 to 1.0 V (forward sweep, labeled '1') and returned to 0 V (reverse sweep, labeled '2') with a sweep rate of 0.3 $Vs^{-1}$ and a step size of 0.01 V (see Figure 2a,b). The current compliance was controlled by an external current limiter of the Keithley 4200-SCS. Pulsed voltage measurements were performed using Keithley 4225-PMU pulse measure units.

### 4.4 | Simulation Model

The JART ECM v1 model [63] is a deterministic compact model. It was used to capture the ECM device switching by tracking the effective tunneling distance $x$ between the active electrode (TE) and the filament tip, which is modulated by filament growth [42, 43]. The device was represented by two parallel branches between the active TE and inert BE: (i) an electronic tunneling path $I_{Tu}$ and (ii) an ionic path $I_{ion}$ that comprised nucleation, redox (electron-transfer) reactions at both interfaces, and ion migration through the switching medium.

The state evolution, i.e., the evolution of the tunnelling distance $x$, is described by Faraday's law [64]:

$$\frac{dx}{dt} = -\frac{M_{Me}}{ze\rho_{m,Me}} j_{ion} \tag{1}$$

where $j_{ion}$ is the ionic current density, $M_{Me}$ is the atomic mass of the deposited active electrode's metal, $z$ is the charge transfer number, and $\rho_{m,Me}$ is its mass density. The nucleation time, which is the time needed to build a pre-filament seed at the inert electrode/switching medium interface, is given as [65, 66]:

$$t_{nuc} = t_{0,nuc} \exp\left(\frac{\Delta G_{nuc}}{k_B T}\right) \exp\left(-\frac{(N_c + \alpha_{nuc})\, ze}{k_B T} \eta_{nuc}\right) \tag{2}$$

Here, $t_{0,nuc}$ denotes the nucleation time prefactor, $\Delta G_{nuc}$ is the nucleation activation energy, $k_B$ is the Boltzmann constant, $T$ is the temperature, $N_c$ is the number of metal atoms needed to achieve a stable nucleation seed, $\alpha_{nuc}$ is the charge transfer coefficient for nucleation, and $\eta_{nuc}$ is the nucleation overpotential. The electron-transfer (redox) processes are given by the Tafel equation [67], a simplified version of the Butler-Volmer equation. At the filament/insulator interface during switching, this equation is as follows:

$$I_{fil} = j_{0,et} A_{fil} \left(\exp\left(-\frac{\alpha_{et} ez}{k_B T} \eta_{fil}\right) - 1\right) \tag{3}$$

whereas at the active electrode/insulator interface during the switching, it reads:

$$I_{ac} = j_{0,et}\, A_{ac} \left(\exp\left(\frac{(1-\alpha_{et})\, ez}{k_B T} \eta_{ac}\right) - 1\right) \tag{4}$$

The respective electron transfer overpotentials are given as $\eta_{fil}$ and $\eta_{ac}$, where $\alpha_{et}$ is the charge transfer coefficient. The introduced areas were defined as $A_{fil} = \pi {r_{fil}}^2$ and $A_{ac} = \pi {r_{ac}}^2$ (with $r_{fil}$ the filament radius and $r_{ac}$ the active electrode radius). The exchange current density in Equations (4) and (5) is portrayed as:

$$j_{0,et} = zeck_{0,et} \exp\left(-\frac{\Delta G_{et}}{k_B T}\right) \tag{5}$$

where the electron transfer activation barrier is denoted as $\Delta G_{et}$, the ion concentration close to the interface is $c$, and the rate constant is $k_{0,et}$. The ion migration through the switching medium is described by the Mott–Gurney hopping:

$$I_{hop} = j_{0,hop}\, A_{is} \sinh\left(\frac{aze}{2k_B T} \frac{\eta_{hop}}{x}\right) \tag{6}$$

with:

$$j_{0,hop} = 2zecaf \exp\left(-\frac{\Delta G_{hop}}{k_B T}\right) \tag{7}$$

$a$ is the mean hopping distance, $f$ the hopping attempt frequency, $\Delta G_{hop}$ the migration barrier, $A_{is}$ the ionic hopping cross-section area (with $r_{is}$ the corresponding radius), and $E = \eta_{hop}/x$ the electric field. The process in the electronic branch is the electronic tunneling, given by a modified Simmons equation [68]:

$$I_{Tu} = C \frac{3\sqrt{2m_{eff}\Delta W_0}}{2x} \left(\frac{e}{h}\right)^2 \exp\left(-\frac{4\pi x}{h}\sqrt{2m_{eff}\Delta W_0}\right) A_{fil} V_{Tu} \tag{8}$$

where $C = 2.7$ [42], $m_{eff} = m_r m_0$, $\Delta W_0$ is the effective tunneling barrier, $h$ is Planck's constant, $V_{Tu}$ is the voltage across the



21991160x, 0, Downloaded from https://advanced.onlinelibrary.wiley.com/doi/10.1002/aelm.202500800 by Universitatsbibliothek RWTH Aachen University, Wiley Online Library on [24/03/2026]. See the Terms and Conditions (https://onlinelibrary.wiley.com/terms-and-conditions) on Wiley Online Library for rules of use; OA articles are governed by the applicable Creative Commons License

tunneling distance, $m_r$ is the relative electron mass, and $m_0$ is the electron's remaining mass.

To model the device's cycle-to-cycle variability, two features were applied within the simulation framework [43, 44]: (i) a simplified version of a previously presented cycle-to-cycle variability model and (ii) stochasticity simulation, both of which are presented in the following.

The cycle-to-cycle variability has been imposed on the parameter filament radius $r_{fil}$; thus, this value differs from cycle to cycle. The corresponding simplified variability model was applied as follows [43]: Before initiating the variability simulation, this model parameter was assigned a truncated Gaussian distribution with a certain standard deviation $r_{fil,\sigma}$ centered at a defined mean $r_{fil}$. Unlike a conventional Gaussian, which allows improbable extreme values, the distribution was truncated by global physical boundaries, $r_{fil,trunc,up}$ and $r_{fil,trunc,low}$, to ensure realistic parameter ranges. A filament radius value $r_{fil,1}$ was drawn randomly from the truncated distributions for one cycle. During SPICE-level simulations, 30 such values ($r_{fil,1} - r_{fil,30}$), one for each cycle, were generated in MATLAB and stored in a text file. This file was imported by the circuit simulator (Spectre), which assigned the tabulated values directly to the compact model written in Verilog-A.

Noise was directly incorporated at each simulation step to account for stochastic effects in the state variable $x$ [43]. While the deterministic update follows Faraday's law [Equation (1)], an additional stochastic term was added immediately after each time step solution. The random update interval was chosen simultaneously. This led to (the tunnelling distance's length at step $k$+1)

$$x_{k+1} = x_k - \frac{M_{Me}}{ze\rho_{m,Me}} j_{ion} \Delta t_{sim,step} \pm \delta \cdot p_{jump} \quad (9)$$

where $\Delta t_{sim,step}$ is the simulation step size, $x_k$ is the tunnelling distance length at step $k$, and $\delta$ is the stochastic amplitude. Typically, $\delta \ll 1$ nm. This choice can be motivated by atomic dimensions: if a single Ag atom ($d_{Ag} = 0.344$ nm, $r_{Ag} = 0.172$ nm) is added or removed, the corresponding average stochastic step is

$$\delta = d_{Ag} \cdot \frac{{r_{Ag}}^2}{{r_{fil}}^2} \quad (10)$$

with, e.g., $r_{fil}$ values of 1.22 nm or 0.8 nm, giving $\delta$ values of 0.0068 nm or 0.0159 nm, respectively. The factor $p_{jump}$ was randomly drawn between 0 and 1 and updated after $w$ steps, where $w$ itself was randomly selected in each iteration.

### Author Contributions

M.C.L. conceived the research concept and designed the project framework. J.L. carried out the material synthesis, Raman analysis, device fabrication, and electrical measurements. K.R. performed the TEM and EDSX analyses. R.W.A. and S.M. provided the models and conducted the simulations. Data analysis was conducted by J.L., R.W.A., S.C., D.B., L.V., J.M., S.M., A.D., and M.C.L. All the authors contributed to the interpretation of the results. J.L. wrote the initial draft, and all the authors revised the manuscript. The work was supervised by A.D., S.M., and M.C.L.


### Acknowledgements

The authors acknowledge support from Dr. Marcus Hans and Prof. Jochen Schneider (StrucMatLab, RWTH Aachen University)

Open access funding enabled and organized by Projekt DEAL.

### Funding

Financial support from the German Federal Ministry of Research, Technology and Space (BMFTR) within the project NEUROTEC 2 (Nos. 16ME0398K, 16ME0399, and 16ME0400) and the NeuroSys "Clusters4Future" initiative (Nos. 03ZU1106AA and 03ZU1106AB), from the European Union's Horizon Europe Research and Innovation Program (via CHIPS-JU) under the project ENERGIZE (101194458), and from the Deutsche Forschungsgemeinschaft (DFG) within the project MEMMEA in SPP 2262 MemrisTec (441918103) and the Emmy Noether Programme (506140715) is gratefully acknowledged.


### Conflicts of Interest

The authors declare no conflicts of interest.

### Data Availability Statement

The data generated and/or analyzed during this study are included in this manuscript and its supplementary material. The raw data will be made available upon reasonable request.

### References


1. M. C. Lemme, D. Akinwande, and C. Huyghebaert, "2D Materials for Future Heterogeneous Electronics," *Nature Communications* 13 (2022): 1392, https://doi.org/10.1038/s41467-022-29001-4.

2. J. Xie, M. N. Patoary, M. A. Rahman Laskar, et al., "Quantum Conductance in Vertical Hexagonal Boron Nitride Memristors With Graphene-Edge Contacts," *Nano Letters* 24 (2024): 2473–2480, https://doi.org/10.1021/acs.nanolett.3c04057.

3. W. Ahn, S. Lee, J. Oh, H. Lee, and S.-Y. Choi, "Crystallinity-Controlled Hexagonal Boron Nitride-Based Memristors for Fully Integrated Reservoir Computing Processors," *Advanced Materials* 37 (2025): 2413640, https://doi.org/10.1002/adma.202413640.

4. S. Jain, S. Li, H. Zheng, L. Li, X. Fong, and K.-W. Ang, "Heterogeneous Integration of 2d Memristor Arrays and Silicon Selectors for Compute-in-Memory Hardware in Convolutional Neural Networks," *Nature Communications* 16 (2025): 2719, https://doi.org/10.1038/s41467-025-58039-3.

5. R. Ge, X. Wu, M. Kim, et al., "Atomristor: Nonvolatile Resistance Switching in Atomic Sheets of Transition Metal Dichalcogenides," *Nano Letters* 18 (2018): 434–441, https://doi.org/10.1021/acs.nanolett.7b04342.

6. X.-D. Li, N.-K. Chen, B.-Q. Wang, et al., "Resistive Memory Devices at the Thinnest Limit: Progress and Challenges," *Advanced Materials* 36 (2024): 2307951, https://doi.org/10.1002/adma.202307951.

7. Y. Lee, Y. Huang, Y.-F. Chang, et al., "Programmable Retention Characteristics in $MoS_2$-based Atomristors for Neuromorphic and Reservoir Computing Systems," *ACS Nano* 18 (2024): 14327–14338, https://doi.org/10.1021/acsnano.4c00333.

8. L. Völkel, D. Braun, M. Belete, et al., "Resistive Switching and Current Conduction Mechanisms in Hexagonal Boron Nitride Threshold Memristors With Nickel Electrodes," *Advanced Functional Materials* 34 (2024): 2300428, https://doi.org/10.1002/adfm.202300428.

9. S. S. Teja Nibhanupudi, A. Roy, D. Veksler, et al., "Ultra-Fast Switching Memristors Based on Two-Dimensional Materials," *Nature Communications* 15 (2024): 2334, https://doi.org/10.1038/s41467-024-46372-y.





2199160x, 0, Downloaded from https://advanced.onlinelibrary.wiley.com/doi/10.1002/aelm.202500800 by Universitatsbibliothek RWTH Aachen University, Wiley Online Library on [24/03/2026]. See the Terms and Conditions (https://onlinelibrary.wiley.com/terms-and-conditions) on Wiley Online Library for rules of use; OA articles are governed by the applicable Creative Commons License

10. Y. Yuan, S. Pazos, J. Li, et al., "On-Chip Atomristors," *Materials Science and Engineering: R: Reports* 165 (2025): 101006, https://doi.org/10.1016/j.mser.2025.101006.

11. R. D. Nikam and H. Hwang, "Atomic Threshold Switch Based on All-2D Material Heterostructures With Excellent Control Over Filament Growth and Volatility," *Advanced Functional Materials* 32 (2022): 2201749, https://doi.org/10.1002/adfm.202201749.

12. F. Huang, C. Ke, J. Li, et al., "Controllable Resistive Switching in $RES_2/WS_2$ Heterostructure for Nonvolatile Memory and Synaptic Simulation," *Advanced Science* 10 (2023): 2302813, https://doi.org/10.1002/advs.202302813.

13. Z. Wang, B. Peng, X. Huang, et al., "Nonvolatile Memristor Based on $WS_2/WSE_2$ van der Waals Heterostructure With Tunable Interlayer Coupling," *Advanced Functional Materials* 35 (2025): 2501372, https://doi.org/10.1002/adfm.202501372.

14. L. Liu, Y. Li, X. Huang, et al., "Low-Power Memristive Logic Device Enabled by Controllable Oxidation of 2D $HfSe_2$ for In-Memory Computing," *Advanced Science* 8 (2021): 2005038, https://doi.org/10.1002/advs.202005038.

15. Y. Li, S. Chen, Z. Yu, et al., "In-Memory Computing using Memristor Arrays With Ultrathin 2D $PdSeO_x$ /$PdSe_2$ Heterostructure," *Advanced Materials* 34 (2022): 2201488, https://doi.org/10.1002/adma.202201488.

16. C. Mahata, D. Ju, T. Das, et al., "Artificial Synapses Based on 2D-Layered Palladium Diselenide Heterostructure Dynamic Memristor for Neuromorphic Applications," *Nano Energy* 120 (2024): 109168, https://doi.org/10.1016/j.nanoen.2023.109168.

17. Y. Lin, W. Wang, R. Li, et al., "Multifunctional Optoelectronic Memristor Based on $CeO_2/MoS_2$ Heterojunction for Advanced Artificial Synapses and Bionic Visual System With Nociceptive Sensing," *Nano Energy* 121 (2024): 109267, https://doi.org/10.1016/j.nanoen.2024.109267.

18. Y. Liu, Y. Huang, and X. Duan, "Van der Waals Integration Before and Beyond Two-Dimensional Materials," *Nature* 567 (2019): 323–333, https://doi.org/10.1038/s41586-019-1013-x.

19. J. Xie, A. E. Yekta, F. A. Mamun, et al., "On-Chip Direct Synthesis of Boron Nitride Memristors," *Nature Nanotechnology* 20 (2025): 1596–1604, https://doi.org/10.1038/s41565-025-01988-z.

20. J. Kim, X. Ju, K.-W. Ang, and D. Chi, "Van der Waals Layer Transfer of 2d Materials for Monolithic 3d Electronic System Integration: Review and Outlook," *ACS Nano* 17 (2023): 1831–1844, https://doi.org/10.1021/acsnano.2c10737.

21. M. Belete, S. Kataria, A. Turfanda, et al., "Nonvolatile Resistive Switching in Nanocrystalline Molybdenum Disulfide With Ion-Based Plasticity," *Advanced Electronic Materials* 6 (2020): 1900892, https://doi.org/10.1002/aelm.201900892.

22. K. Ranganathan, M. Fiegenbaum-Raz, and A. Ismach, "Large-Scale and Robust Multifunctional Vertically Aligned $MoS_2$ Photo-Memristors," *Advanced Functional Materials* 30 (2020): 2005718, https://doi.org/10.1002/adfm.202005718.

23. D. Dev, A. Krishnaprasad, M. S. Shawkat, et al., "2D $MoS_2$ -Based Threshold Switching Memristor for Artificial Neuron," *IEEE Electron Device Letters* 41 (2020): 936–939, https://doi.org/10.1109/LED.2020.2988247.

24. D. Dev, M. S. Shawkat, A. Krishnaprasad, Y. Jung, and T. Roy, "Artificial Nociceptor Using 2d $MoS_2$ Threshold Switching Memristor," *IEEE Electron Device Letters* 41 (2020): 1440–1443, https://doi.org/10.1109/LED.2020.3012831.

25. S. J. Kim, T. H. Lee, J.-M. Yang, et al., "Vertically Aligned Two-Dimensional Halide Perovskites for Reliably Operable Artificial Synapses," *Materials Today* 52 (2022): 19–30, https://doi.org/10.1016/j.mattod.2021.10.035.

26. J. Lee, R. W. Ahmad, S. Cruces, et al., "Threshold Switching in Vertically Aligned $mos_2/SiO_x$ Heterostructures Based on Silver Ion Migration," *npj 2D Materials and Applications* 9 (2025): 86, https://doi.org/10.1038/s41699-025-00614-9.

27. M. Lanza, A. Sebastian, W. D. Lu, et al., "Memristive Technologies for Data Storage, Computation, Encryption, and Radio-Frequency Communication," *Science* 376 (2022): abj9979, https://doi.org/10.1126/science.abj9979.

28. W. Wang, M. Wang, E. Ambrosi, et al., "Surface Diffusion-Limited Lifetime of Silver and Copper Nanofilaments in Resistive Switching Devices," *Nature Communications* 10 (2019): 81, https://doi.org/10.1038/s41467-018-07979-0.

29. Y. Ji, L. Wang, Y. Long, et al., "Ultralow Energy Adaptive Neuromorphic Computing Using Reconfigurable Zinc Phosphorus Trisulfide Memristors," *Nature Communications* 16 (2025): 6899, https://doi.org/10.1038/s41467-025-62306-8.

30. R. Waser, R. Dittmann, G. Staikov, and K. Szot, "Redox-Based Resistive Switching Memories—Nanoionic Mechanisms, Prospects, and Challenges," *Advanced Materials* 21 (2009): 2632–2663, https://doi.org/10.1002/adma.200900375.

31. R. Xu, H. Jang, M.-H. Lee, et al., "Vertical $MoS_2$ Double-Layer Memristor With Electrochemical Metallization as an Atomic-Scale Synapse With Switching Thresholds Approaching 100 Mv," *Nano Letters* 19 (2019): 2411–2417, https://doi.org/10.1021/acs.nanolett.8b05140.

32. L. Völkel, R. W. Ahmad, A. Bestaeva, et al., "Influence of Humidity on the Resistive Switching of Hexagonal Boron Nitride-Based Memristors," *npj 2D Materials and Applications* 9 (2025): 41, https://doi.org/10.1038/s41699-025-00566-0.

33. S. A. Chekol, S. Menzel, R. W. Ahmad, R. Waser, and S. Hoffmann-Eifert, "Effect of the Threshold Kinetics on the Filament Relaxation Behavior of Ag-Based Diffusive Memristors," *Advanced Functional Materials* 32 (2022): 2111242, https://doi.org/10.1002/adfm.202111242.

34. S. A. Chekol, S. Menzel, R. Waser, and S. Hoffmann-Eifert, "Strategies to Control the Relaxation Kinetics of Ag-Based Diffusive Memristors and Implications for Device Operation," *Advanced Electronic Materials* 8 (2022): 2200549, https://doi.org/10.1002/aelm.202200549.

35. M. Kaniselvan and Y. Yoon, "Strain-Tuning $PtSe_2$ for High On-Current Lateral Tunnel Field-Effect Transistors," *Applied Physics Letters* 119 (2021): 073102, https://doi.org/10.1063/5.0053789.

36. Y. Gu, M. I. Serna, S. Mohan, et al., "Sulfurization Engineering of One-Step Low-Temperature $MoS_2$ and $WS_2$ Thin Films for Memristor Device Applications," *Advanced Electronic Materials* 8 (2022): 2100515, https://doi.org/10.1002/aelm.202100515.

37. S. Lan, F. Zheng, C. Ding, et al., "Advancing High-Performance Memristors Enabled by Position-Controlled Grain Boundaries in Controllably Grown Star-Shaped $mos_2$," *Nano Letters* 24 (2024): 15388–15395, https://doi.org/10.1021/acs.nanolett.4c04642.

38. M. D. Ganeriwala, D. Luque-Jarava, F. Pasadas, et al., "Effect of Grain Boundaries on Metal Atom Migration and Electronic Transport in 2D TMD-based Resistive Switches," *Nanoscale* 17 (2025): 13797–13807, https://doi.org/10.1039/D4NR05321D.

39. T. Lehenkari, S.-D. Huang, K. Kordas, and H.-P. Komsa, "First-Principles Study of Ag, Au, Cu, and Li Defects in $MoS_2$ and Their Application to Memristors," *Physical Review Materials* 9 (2025): 014001, https://doi.org/10.1103/PhysRevMaterials.9.014001.

40. K. Ran, J. Jo, S. Cruces, et al., "Unraveling the Dynamics of Conductive Filaments in $MoS_2$-based Memristors by Operando Transmission Electron Microscopy," *Nature Communications* 16 (2025): 7433, https://doi.org/10.1038/s41467-025-62592-2.

41. S. Cruces, M. D. Ganeriwala, J. Lee, et al., "Volatile $MoS_2$ Memristors With Lateral Silver Ion Migration for Artificial Neuron Applications," *Small Science* 5 (2025): 240052, https://doi.org/10.1002/smsc.202400523.

42. S. Menzel, S. Tappertzhofen, R. Waser, and I. Valov, "Switching Kinetics of Electrochemical Metallization Memory Cells," *Physical Chemistry Chemical Physics* 15 (2013): 6945, https://doi.org/10.1039/C3CP50738F.



2199160x, 0, Downloaded from https://advanced.onlinelibrary.wiley.com/doi/10.1002/aelm.202500800 by Universitatsbibliothek RWTH Aachen University, Wiley Online Library on [24/03/2026]. See the Terms and Conditions (https://onlinelibrary.wiley.com/terms-and-conditions) on Wiley Online Library for rules of use; OA articles are governed by the applicable Creative Commons License

43. R. W. Ahmad, R. Waser, F. Maudet, O. Toprak, C. Dubourdieu, and S. Menzel, "Variability-Aware Modeling of Electrochemical Metallization Memory Cells," *Neuromorphic Computing and Engineering* 4 (2024): 034007, https://doi.org/10.1088/2634-4386/ad57e7.

44. R. W. Ahmad and S. Menzel, "JART ECM v1 Var," (2025), https://doi.org/10.26165/JUELICH-DATA/WHSSZA.

45. M. Belete, S. Kataria, U. Koch, et al., "Dielectric Properties and Ion Transport in Layered $MoS_2$ Grown by Vapor-phase Sulfurization for Potential Applications in Nanoelectronics," *ACS Applied Nano Materials* 1 (2018): 6197–6204, https://doi.org/10.1021/acsanm.8b01412.

46. H. Liu, A. Iskander, N. L. Yakovlev, and D. Chi, "Anomalous $SiO_2$ Layer Formed on Crystalline $MoS_2$ Films Grown on Si by Thermal Vapor Sulfurization of Molybdenum at Elevated Temperatures," *Materials Letters* 160 (2015): 491–495, https://doi.org/10.1016/j.matlet.2015.08.042.

47. A. Krishnaprasad, D. Dev, S. S. Han, et al., "MoS2 Synapses With Ultra-Low Variability and Their Implementation in Boolean Logic," *ACS Nano* 16 (2022): 2866–2876, https://doi.org/10.1021/acsnano.1c09904.

48. G. Deokar, N. S. Rajput, P. Vancsó, et al., "Large Area Growth of Vertically Aligned Luminescent $MoS_2$ Nanosheets," *Nanoscale* 9 (2017): 277–287, https://doi.org/10.1039/C6NR07965B.

49. D. Kong, H. Wang, J. J. Cha, et al., "Synthesis of $MoS_2$ and $MoSe_2$ Films With Vertically Aligned Layers," *Nano Letters* 13 (2013): 1341–1347, https://doi.org/10.1021/nl400258t.

50. S. Cruces, M. D. Ganeriwala, J. Lee, et al., "Volatile and Nonvolatile Resistive Switching in Lateral 2d Molybdenum Disulfide-Based Memristive Devices," *Nano Letters* 25 (2025): 12455–12462, https://doi.org/10.1021/acs.nanolett.5c01992.

51. K. Kim, J. G. Lim, S. M. Hu, et al., "Multifilamentary Switching of Cu/$SiO_x$ Memristive Devices With a Ge-Implanted a-Si Underlayer for Analog Synaptic Devices," *NPG Asia Materials* 15 (2023): 48, https://doi.org/10.1038/s41427-023-00495-8.

52. K. Liu, L. Qin, X. Zhang, et al., "Interfacial Redox Processes in Memristive Devices Based on Valence Change and Electrochemical Metallization," *Faraday Discussions* 213 (2019): 41–52, https://doi.org/10.1039/C8FD00113H.

53. X. F. Lu, Y. Zhang, N. Wang, et al., "Exploring Low Power and Ultrafast Memristor on p-Type van der Waals SnS," *Nano Letters* 21 (2021): 8800–8807, https://doi.org/10.1021/acs.nanolett.1c03169.

54. Y. Fa, M. Buttberg, K. Ran, et al., "Intermediate Resistive State in Wafer-Scale Vertical $MoS_2$ Memristors Through Lateral Silver Filament Growth for Artificial Synapse Applications," *Advanced Functional Materials* (2025): 26682, https://doi.org/10.1002/adfm.202526682.

55. Z. Wang, M. Rao, R. Midya, et al., "Threshold Switching of Ag or Cu in Dielectrics: Materials, Mechanism, and Applications," *Advanced Functional Materials* 28 (2018): 1704862, https://doi.org/10.1002/adfm.201704862.

56. A. Bricalli, E. Ambrosi, M. Laudato, M. Maestro, R. Rodriguez, and D. Ielmini, "$SiO_x$-Based Resistive Switching Memory (RRAM) for Crossbar Storage/Select Elements With High On/off Ratio," in *IEEE International Electron Devices Meeting (IEDM)*, (San Francisco, CA, USA 2016), https://doi.org/10.1109/IEDM.2016.7838344.

57. J. J. Yang, D. B. Strukov, and D. R. Stewart, "Memristive Devices for Computing," *Nature Nanotechnology* 8 (2013): 13–24, https://doi.org/10.1038/nnano.2012.240.

58. I. H. Im, S. J. Kim, and H. W. Jang, "Memristive Devices for New Computing Paradigms," *Advanced Intelligent Systems* 2 (2020): 2000105, https://doi.org/10.1002/aisy.202000105.

59. W. Wang, E. Covi, Y.-H. Lin, et al., "Switching Dynamics of Ag-Based Filamentary Volatile Resistive Switching Devices—Part II: Mechanism and Modeling," *IEEE Transactions on Electron Devices* 68 (2021): 4342–4349, https://doi.org/10.1109/TED.2021.3095033.

60. H. Abbas, J. Li, and D. S. Ang, "Conductive Bridge Random Access Memory (CBRAM): Challenges and Opportunities for Memory and Neuromorphic Computing Applications," *Micromachines* 13: 725, https://doi.org/10.3390/mi13050725.

61. C. Stern, S. Grinvald, M. Kirshner, et al., "Growth Mechanisms and Electronic Properties of Vertically Aligned mos2," *Scientific Reports* 8 (2018): 16480, https://doi.org/10.1038/s41598-018-34222-z.

62. A. Bondi, "Van der Waals Volumes and Radii," *The Journal of Physical Chemistry* 68 (1964): 441–451, https://doi.org/10.1021/j100785a001.

63. S. Menzel and C. Bengel, JART ECM v1 (2025), https://doi.org/10.26165/JUELICH-DATA/4F3ITW.

64. M. Faraday, "VI. Experimental Researches in Electricity.-Seventh Series," *Philosophical Transactions of the Royal Society of London* 124 (1834): 77–122, https://doi.org/10.1098/rstl.1834.0008.

65. R. Soni, P. Meuffels, G. Staikov, et al., "On the Stochastic Nature of Resistive Switching in cu Doped $Ge_{0.3}Se_{0.7}$ Based Memory Devices," *Journal of Applied Physics* 110 (2011): 054509, https://doi.org/10.1063/1.3631013.

66. E. Budevski, G. Staikov, and W. J. Lorenz, *Electrochemical Phase Formation and Growth* (VCH, 1996), https://doi.org/10.1002/9783527614936.

67. C. H. Hamann, A. Hamnett, and W. Vielstich, *Electrochemistry* (Wiley-VCH, 2007).

68. J. G. Simmons, "Generalized Formula for the Electric Tunnel Effect Between Similar Electrodes Separated by a Thin Insulating Film," *Journal of Applied Physics* 34 (1963): 1793–1803, https://doi.org/10.1063/1.1702682.

## Supporting Information

Additional supporting information can be found online in the Supporting Information section.

**Supporting File**: aelm70332-sup-0001-SuppMat.docx.



2199160x, 0, Downloaded from https://advanced.onlinelibrary.wiley.com/doi/10.1002/aelm.202500800 by Universitatsbibliothek RWTH Aachen University, Wiley Online Library on [24/03/2026]. See the Terms and Conditions (https://onlinelibrary.wiley.com/terms-and-conditions) on Wiley Online Library for rules of use; OA articles are governed by the applicable Creative Commons License